



Analysis of Local Creep Strain Field and Cracking Process in Claystone by X-Ray Micro-Tomography and Digital Volume Correlation

Hai-Ling Shi^{1,2} · Jerome Hosdez² · Thomas Rougelot² · Shou-Yi Xie² · Jian-Fu Shao^{1,2} · Jean Talandier³

Received: 21 May 2020 / Accepted: 13 January 2021 / Published online: 3 February 2021
© The Author(s), under exclusive licence to Springer-Verlag GmbH, AT part of Springer Nature 2021

Abstract

X-ray micro-tomography (XMT) is an efficient technique for non-destructive imaging of morphological structures. It is suitable for monitoring local displacement fields of heterogeneous materials. Digital volume correlation (DVC) methods are widely used for the quantification of local strain fields from highly contrasted XMT images. The aim of this work is to investigate strain localization and cracking process in a hard clayey rock. For this purpose, three-dimensional images have been taken by in situ X-ray micro-tomography on a tested sample under different loading levels and time steps. These images are analyzed with a DVC based method to calculate both local strain fields and averaged global strains. In particular, the progressive localization of strain field with applied stress and creep time is investigated in relation with material heterogeneities. It is found that the strain field localization as well as the cracking process is clearly influenced by the presence of stiff inclusions, pores, weak clayey zones and layered microscopic structure of claystone.

Keywords X-ray micro-tomography · Digital volume correlation · Local strain · In situ creep test · Clayey rock

1 Introduction

Clayey rocks have been widely investigated in geological and engineering practices. As a current example, clayey rocks are selected as potential geological barriers in several countries for underground disposal of radioactive waste (Armand et al. 2014, 2017). A high number of experimental studies, at different scales, have been performed for the characterization of mineralogy, micro-structure and thermo-hydrmechanical (THM) properties. It is found that clayey rocks are heterogeneous materials containing different kinds of mineral inclusions and pores at different scale (Robinet et al. 2012; Bennett et al. 2015). Their macroscopic THM properties are clearly affected by the mineralogy and

heterogeneities (Hu et al. 2014; Liu et al. 2018), as well as by water content (Hu et al. 2014; Yang et al. 2013; Liu et al. 2018) and temperature (Chen et al. 2014; Menaceur et al. 2015; Liu et al. 2019). Most clayey rocks also exhibit a clear initial anisotropy so that their THM properties are dependent on loading orientation (Zhang et al. 2012; Yang et al. 2013; Liu et al. 2015b). Due to strong heterogeneity, cracking induced by THM loading is also an important process of many clayey rocks (Wang et al. 2015). On the other hand, for the long term safety analysis of geological disposal of radioactive waste, time-dependent deformation of clayey rocks is a primordial property to be taken into account (Liu et al. 2015b). For instance, creep deformation can be a driving factor for the time-dependent cracking process through closure of excavation-induced cracks or creation of new cracks, generating variation of transport properties such as permeability (Liu et al. 2015a, 2016). Conversely, creep deformation is controlled by stress fields and fluid pressure. Therefore, long term evolutions of fluid pressure, stress fields and creep deformation are intimately coupled. On the other hand, the creep deformation in clayey rocks is generally related to the clay matrix. Standard macroscopic creep tests provide overall creep strains but are not able to identify the local creep strain field inside the clay matrix. Therefore, microscopic tests become a crucial issue.

✉ Jian-Fu Shao
jian-fu.shao@polytech-lille.fr

¹ Key Laboratory of Ministry of Education on Safe Mining of Deep Metal Mines, College of Resources and Civil Engineering, Northeastern University, Shenyang 110819, China

² UMR9013-LaMcube-Laboratoire de Mécanique Multiphysique et Multiéchelle, Univ. Lille, CNRS, Centrale Lille, 59000 Lille, France

³ Andra, 92298 Chatenay Malabry, France

During the last decades, different kinds of imaging techniques have been developed to capture local displacement fields in heterogeneous materials. Among these techniques, three-dimensional (3D) X-ray micro-tomography imaging has become one of the most widely used. The main principles of computerized tomographic imaging can be found in (Kak and Slaney 2001). This technique has also successfully applied to rock-like materials, initial for the post-mortem analysis of deformation and cracking in tested samples (Chu et al. 1985; Kawakata et al. 1999; Otani et al. 2000; Bornert 2010; Chen et al. 2014; Yang et al. 2016). More recently, new experimental devices have been designed allowing the realization of in situ tests with real time micro-tomography monitoring (Viggiani et al. 2013; Pardoen et al. 2020). Multi-modal X-Ray and neutron tomographies have even been combined to study the dynamics of water absorption in claystone (Stavropoulou et al. 2020). However, in situ creep tests with XMT monitoring have so far been rarely performed on rocks.

High-resolution and highly contrast images obtained from micro-tomography and all other observation techniques can be analyzed by different mathematical methods to quantify strain fields in selected observation zones. Methods based on digital image correlation digital (DIC) for 2D problems and digital volume correlation (DVC) for 3D problems are the most widely used. A recent review on DVC methods can be found in (Buljac et al. 2018). The combination of XMT imaging and DVC or DIC based methods has successfully been used for the determination of local displacement and strain fields in different kinds of materials (Besnard et al. 2006; Stock 2008; Bornert 2010; Desbois et al. 2017). In some studies, these methods have been used for the characterization of strain localization and cracking processes (Viggiani et al. 2004; Bauer et al. 2006; Desrues et al. 2010; Lenoir et al. 2007; Mao et al. 2019).

The main objective of this study is to characterize the full strain field, the strain localization as well as cracking process in a hard clayey rock sample. A series of uniaxial compression creep tests are performed with XMT monitoring and the obtained images are analyzed by a DVC based method. The present paper is organized as follows. The specific experimental procedure for creep tests with XMT imaging and DVC calculation is first presented. The obtained experimental results are then presented and discussed in terms of average strains, local strain fields and strain localization as well as induced cracks. The emphasis is put on the analysis of strain localization and of cracking process in relation with the material microstructure and mineralogy.

2 Materials and Methods

2.1 Material and Sampled Preparation

The tested material is the Callovo-Oxfordian (COx) claystone cored at the Underground Research Laboratory (URL) at Bure, operated by the French national agency for radioactive waste management (ANDRA). Based on previous studies (Robinet et al. 2012), the COx claystone is mainly constituted of clay minerals, calcite, quartz and other secondary minerals. The clay fraction is about 40–45%, carbonate (mostly calcite) about 25–35% and quartz about 30%. The minor minerals include pyrite and siderite. The natural water content of the stratum ranges between 5 and 8% (Gasc-Barbier et al. 2004; Armand et al. 2017).

To characterize representative mechanical behaviors of material, the tested sample should be a representative volume element (RVE). That means that the size of sample should be large enough with respect to the size of heterogeneities. At the same time, to get high resolution images by using XMT, the sample size should be as small as possible. For the tested COx claystone, the average size of calcite and quartz grains is about a few hundreds micrometers (Robinet et al. 2012). A reasonable compromise is here adopted. The average size of cylindrical sample used in in situ creep tests is 4.96 mm in diameter and 9.54 mm in length. The emphasis of this study is put on the characterization of creep strain field and cracking process. It is known that the mechanical properties of clayey rocks are dependent on loading orientation with respect to bedding planes. However, in the present study, the emphasis is put on the cracking process and local strain localization in the COx claystone for a given loading orientation. The length axis of the tested sample is chosen to be perpendicular to the stratum or bedding planes. With this choice, the consequence of compaction deformation of bedding planes is expected to be enhanced. The influence of loading orientation with respect to material anisotropy will be investigated in future studies.

More precisely, the tested sample is prepared from original large cores of about 300 mm in length and 79 mm in diameter. An intermediate cylindrical sample with a diameter of about 10 mm is first drilled from the large cores (Reference EST58125). Then the final small sample with a diameter of about 5 mm is carefully cut by using a spiral turning machine. The upper and lower end faces of specimens are carefully cut and polished to obtain a good parallelism. All the sample preparation procedure is completed in the natural air condition and the lateral surface of sample are covered with a plastic film, to minimize the modification of water saturation state. The mass of each

Fig. 1 Intermediate cylindrical cores and final prepared claystone sample

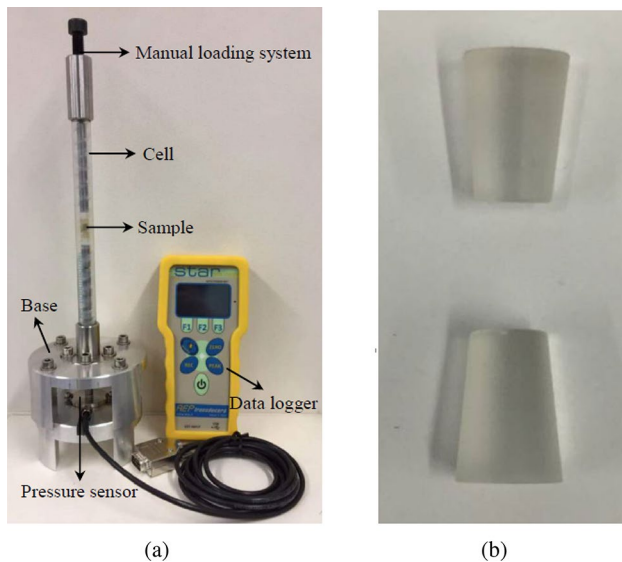
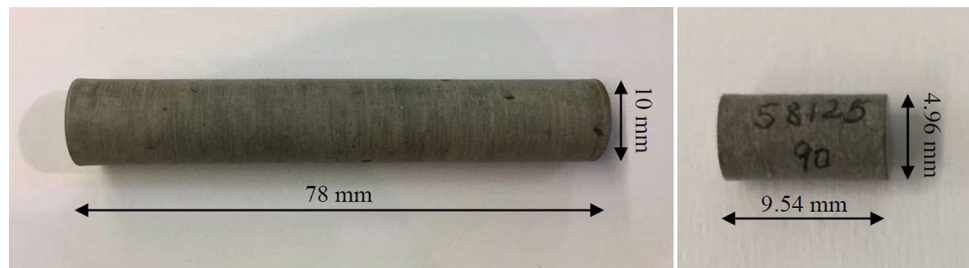


Fig. 2 **a** Overall view of creep test device, **b** translucent polycarbonate bases

prepared sample is measured at the end of preparation and its water content is estimated by using the reference values of dry density and porosity of the COx claystone (Robinet et al. 2012). Their average value is about $4.5 \pm 0.5\%$. An example of prepared sample is shown in Fig. 1.

2.2 Creep Test Device

To realize in situ creep tests with X-ray micro-tomography imaging, a new experimental device is here developed. As shown in Fig. 2a, the designed device includes a long cell, a manual axial loading system, a base, a force sensor and a data logger. The long cell is made of polycarbonate with a high light transmissibility for X-ray. It also has a good mechanical stability. The force sensor has an accuracy of 0.01 kg and a range of 0–100 kg. For the specimens with a diameter of 4–5 mm studied here, the maximum of axial stress generated is about 60–80 MPa. As shown in Fig. 2b, the claystone sample is sandwiched at the middle part of cell by a pair of translucent polycarbonate bases to minimize the friction at the upper and lower surface with loading system. The axial stress is increased as slowly as possible and is

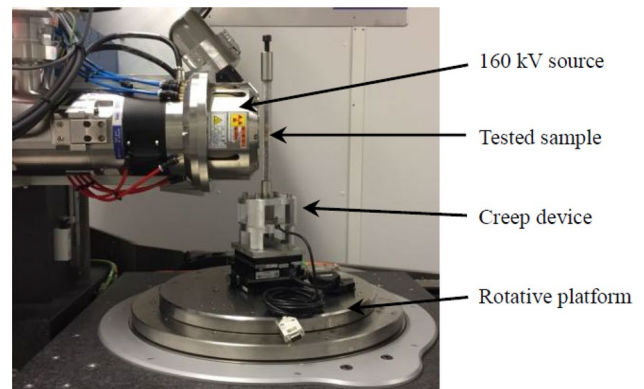


Fig. 3 Picture of X-ray micro-tomography platform (ISIS4D)

monitored by the force sensor. During creep stage, the axial force is regularly adjusted to keep the loading constant. This study focuses on uniaxial compression creep test. Additional experiments are ongoing to investigate the triaxial compression creep behaviour of such a material.

2.3 X-Ray Micro-Tomography

Laboratory X-ray micro-tomography was conducted at the In Situ Innovative Set-ups under X-ray micro-tomography (ISIS4D) platform (Limodin et al. 2013), as shown in Fig. 3. This platform contains a computed tomography system Ultra Tom manufactured by RX solutions. In the present study, a 100 kV acceleration voltage is selected with a filament current of $45 \mu\text{A}$. The claystone sample is placed on the rotating stage between the X-ray source and a flat panel detector of 1874×1496 pixels. A voxel size of $4.5 \mu\text{m}$ is obtained for a claystone sample of 4–5 mm in diameter. About 1440 radiography pictures are taken when the sample is rotated through 360° along its vertical axis. Reconstruction of tomographic data is performed with a filtered back-projection algorithm using the X-act software (Kak and Slaney 2001).

2.4 Digital Volume Correlation

Three-dimensional digital volume correlation (DVC) methods are an extension of the two-dimensional digital image

correlation (DIC) methods. Significant advances have been archived since the end of 1990s and these methods are now widely used for quantitative treatment and analysis of 2D and 3D images. The basic idea is to compare two images of the same zone between two subsequent states, and then to calculate the displacement and strain fields in the zone by searching for the best match between the images. More detailed description of digital image correlation methods can be found in (Kak and Slaney 2001). Only a short review is presented here.

Each image is identified by its gray scale function representing the volume of the sample. Let f denoting the reference 3D image taken before the deformation, while g the deformed 3D image taken after the deformation. In the present study, we use the optical flow equation, which assumes that the gray scale variations are only due to the displacement of the material point. Therefore, the initial and deformed images can be linked by the following relation (Besnard et al. 2006):

$$g(\vec{x}) = f[\vec{x} + \vec{v}(\vec{x})] \quad (1)$$

where \vec{x} is the vector denoting the position of the voxel and \vec{v} is the related displacement vector.

In the present study, a digital image correlation platform called YADICS, developed at Laboratoire de Mécanique de Lille (Lille, France) is used. This platform is based on C++, and optimized to process large 3D volumes in a limited time. Correlation is based on a multi-scale resolution strategy allowing save treatment time as the image contains much fewer voxels at the first resolution level. The correlation calculation is a sequence of optical flow elastic transform based on finite elements method. In the present case, several scales, i.e. resolutions, are employed; the coarsest one with a 'macro' voxel, which is averaged over $2^5 \times 2^5 \times 2^5$ voxels while the full resolution image corresponds to a volume of $2^0 \times 2^0 \times 2^0$. This scheme can reduce the problem size and thus avoids some local minimum traps. For easy and fast convergence at the coarsest scales, only global transformations are searched for, using optical flow integrated (OFI) algorithm while at the finest scales, the more computing intensive optical flow finite element methods (OFFEM) algorithm is adopted to compute local

displacements. Therefore, due to this multi-scale strategy, the correlation sequence per image couple is defined with the following analysis sequence: OFI_H, OFI_H, OFI_H, OFFEM, OFFEM, OFFEM and OFFEM.

Choosing the most suitable element size is very important for the results of DVC calculation. The results of the local strain calculation show a diffusion phenomenon, i.e., the larger the element size, the more obvious the diffusion phenomenon around the local deformation. An example is shown in Fig. 4. Local strain fields are calculated by using isotropic elements of different sizes respectively containing 8, 16 and 32 voxels. It is clear that the obtained results are strongly sensitive to element size. In particular, the strain localization cannot be correctly captured by large elements.

The uncertainty of displacement field is widely used as a parameter to evaluate the accuracy of calculations with DVC methods. This uncertainty is calculated by the standard deviation of the displacement between the two pictures. One is at the reference position and the other translated by 20 microns. Then, the standard deviation of the displacement field is calculated for all the components in three directions. In Fig. 5, one shows the evolution of uncertainty for the three displacement components when the element size varies from 4 to 64 voxels. It is seen

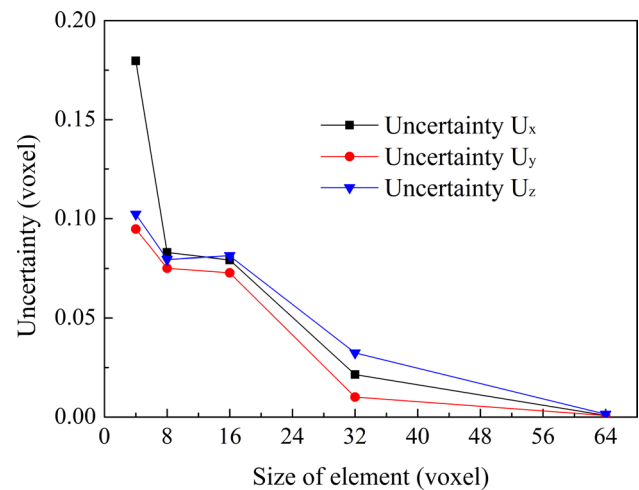
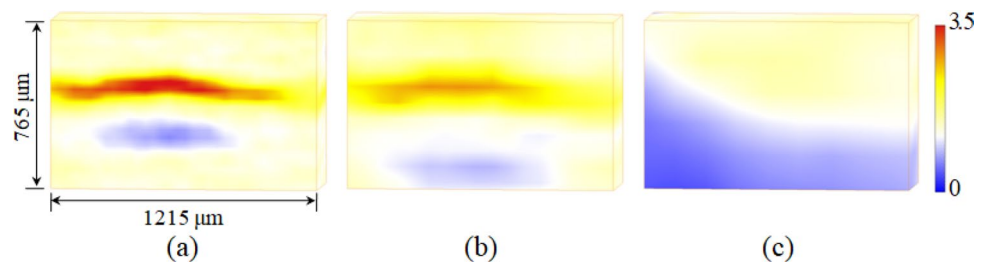


Fig. 5 Variations of uncertainty for three components of displacement with different element sizes in DVC calculations

Fig. 4 Dependency of calculated von Mises equivalent strain field (%) on element size: **a** 8 voxels, **b** 16 voxels and **c** 32 voxels



that the spatial resolutions considered here give quite good results of three-dimensional displacement field. It is noticed that the values of uncertainty obtained here are of the same order of magnitude as that found in previous studies (Wang et al. 2016; Li et al. 2017). Although the uncertainty for high spatial resolution is several times higher than that of low resolution, the description of strain localization process is much better. Considering together the results of strain localization, the time cost of the DVC calculations and the uncertainty in displacement field, the element size with 8 voxels is selected in this study for the DVC analysis of all creep tests.

2.5 Loading and Monitoring Procedure

Based on a preliminary test on a typical sample, the uniaxial compression strength of the studied claystone is about 38 MPa. Based on this value, five stress levels are selected for performing uniaxial creep tests, namely 14.20, 20.79, 25.46, 32.66 and 36.0 MPa, respectively corresponding to 40, 60, 70, 90 and 95% of the uniaxial compression strength. According to some previous studies (Liu et al. 2015b), the creep rate of COx claystone drops to 10^{-9} /s after 400 hours (approximately 2.5 weeks) (loaded at 50% of peak strength). Here each creep step is maintained at least for 3 weeks or until failure of the sample.

The creep cell is kept in a chamber where the temperature is regulated ($19.5 \pm 0.5^\circ\text{C}$) and the desiccation of the sample is prevented by the design of the creep device, which limits water exchange with the environment. The tested sample was wrapped in a rubber sleeve with an inner diameter of 5 mm. In addition, the small size of the sample made it difficult to collect a complete failed sample. We tried to measure the water content of the failed sample and found a small amount of moisture loss, about 12%. Micro-tomography scans are taken during each creep step. To capture the main physical processes to be considered at a relevant scale, the voxel size is an important parameter. In the present study, the emphasis is put on the characterization of creep strain localization and cracking process by taking into account the influence of mineral inclusions and pores. Based on the average size of these inclusions (a few hundreds micrometers) and the size of sample, the voxel size used here is about $4.5 \mu\text{m}$. With this resolution, it is possible to determine the positions of main mineral grains in the studied sample. As shown in Fig. 6, the principal mineral components of claystone at the sample scale are identified by gray-scale images. Further, to capture the progressive cracking process at the subsequent creep steps, four horizontal slices perpendicular to the sample axis are selected and shown in Fig. 7. The evolutions of microstructure on these selected slices are analyzed at the different loading steps.

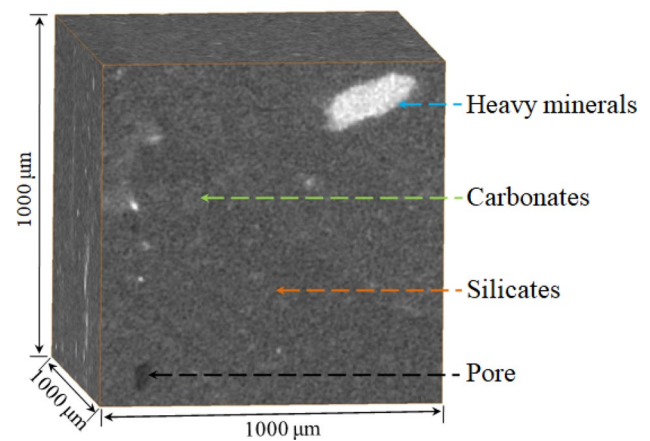


Fig. 6 Simplified view of distribution of main mineral components of claystone

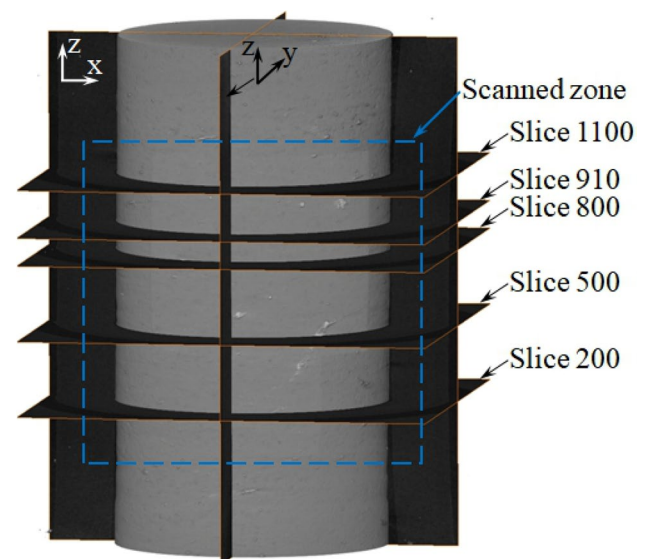


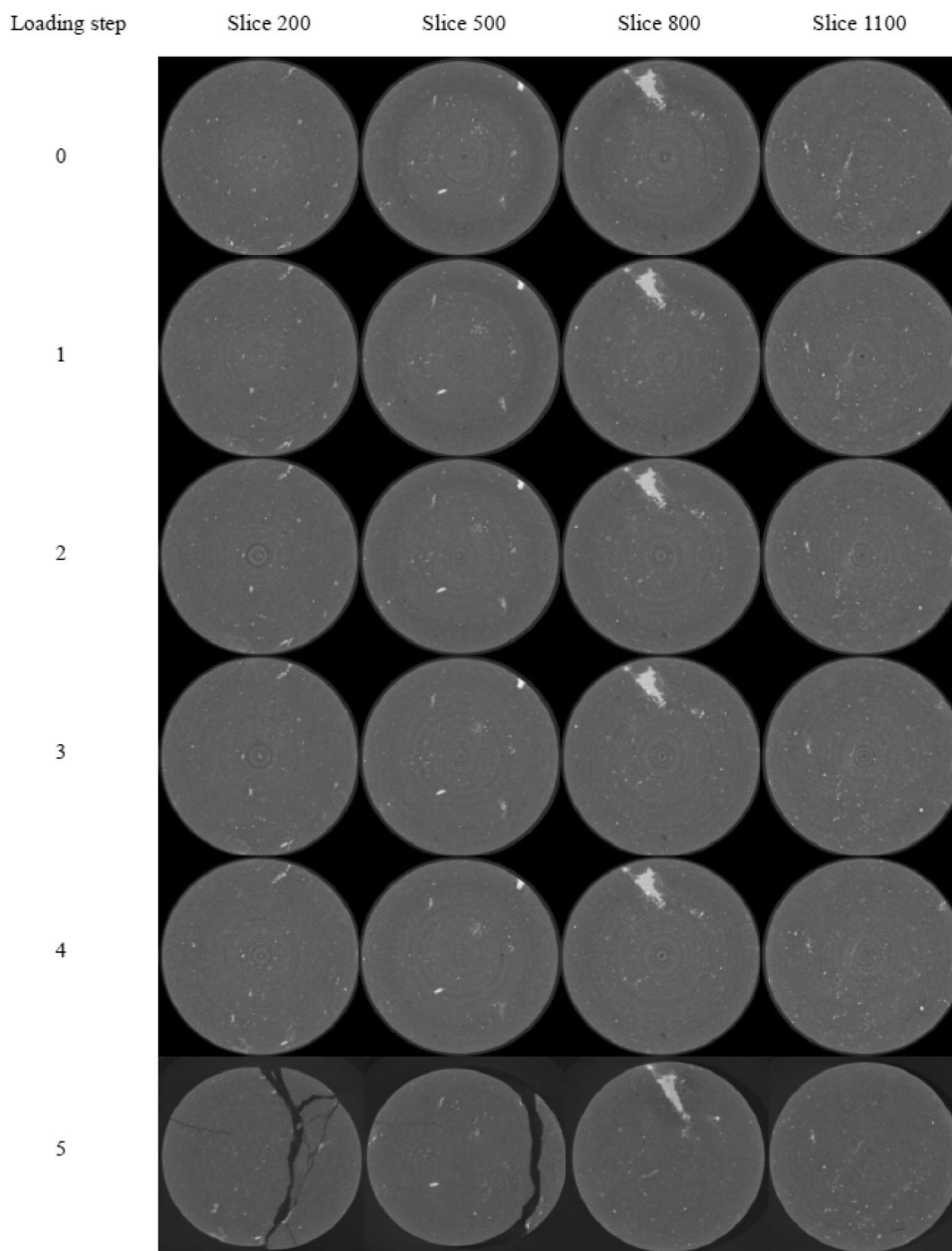
Fig. 7 Positions of selected slices in claystone sample for cracking analysis at different loading steps

3 Cracking Process and Averaged Creep Deformation

3.1 Analysis of Cracking Process

In Fig. 8, one shows the tomographic reconstruction of the selected four slices at five creep loading steps. The step 0 (axial stress = 0) is the initial state and the step 5 (axial stress = 36 MPa) is the last one leading to failure of sample. On these slices, the grey levels represent the attenuation to X-ray and light colors are related to materials with high density. Thus the white zones in images correspond to heavy minerals, e.g., pyrite and siderite. Their movements

Fig. 8 Tomographic reconstruction of four selected horizontal slices in sample EST58125 at different loading steps



during loading steps can be identified. But it is hard to capture the evolution of cracking process during the first four steps. Only at the last loading step, one clearly observes the generated fractures on the slices 200 and 500 located in the lower part of sample. It seems that the failure of sample occurs in a brittle manner when the applied stress is close to the estimated uniaxial compression strength. In Fig. 9, one shows the reconstruction of two longitudinal slices parallel to the longitudinal axis respectively at the initial and failed states. Due to the applied compressive axial stress, the length of sample is clearly compacted. Further, these slices show again that most cracks initiate around from the bottom surface and extend to the middle

part of sample. The arrows with solid lines indicate two major conjugated cracks, while the arrows with dashed lines show the cracks intersecting the major cracks. The absence of the expected vertical through cracks may be due to the loading orientation being perpendicular to the bedding planes.

The three-dimensional tomographic reconstruction of the failed sample is presented in Fig. 10. The distribution and shape of cracks are clearly displayed. In consistency with the previous 2D slices, the 3D image confirms that almost all visible cracks are found in the lower half region of sample and many of them pass through the lower surface. Most major cracks propagate upward inside the sample. It is not

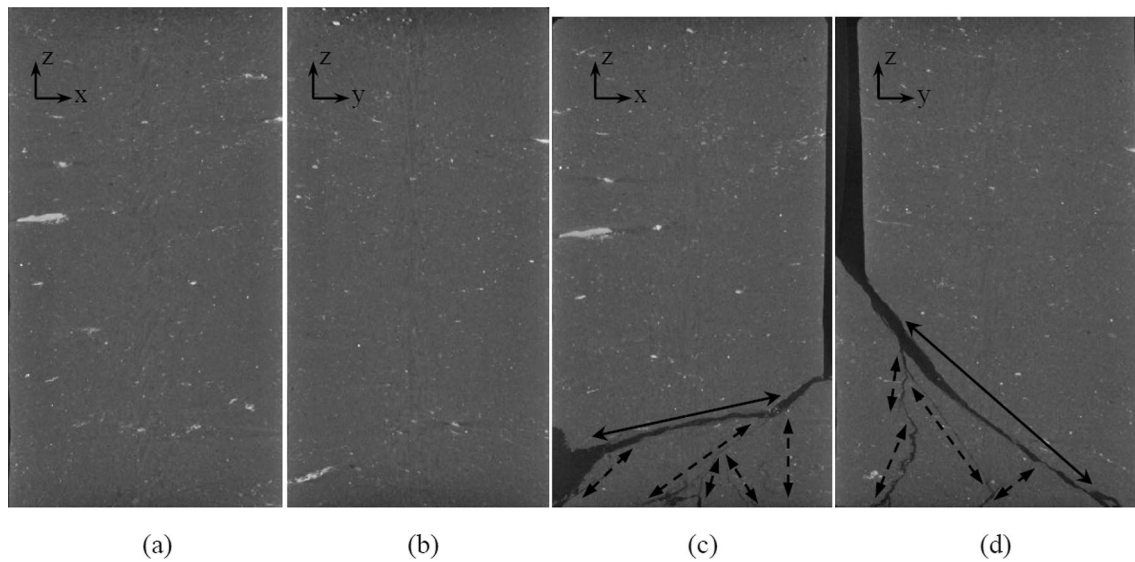


Fig. 9 Tomographic reconstruction of two longitudinal slices at initial state (a) and (b) and at failed state (c) and (d), slices a and b, c and d are perpendicular to each other

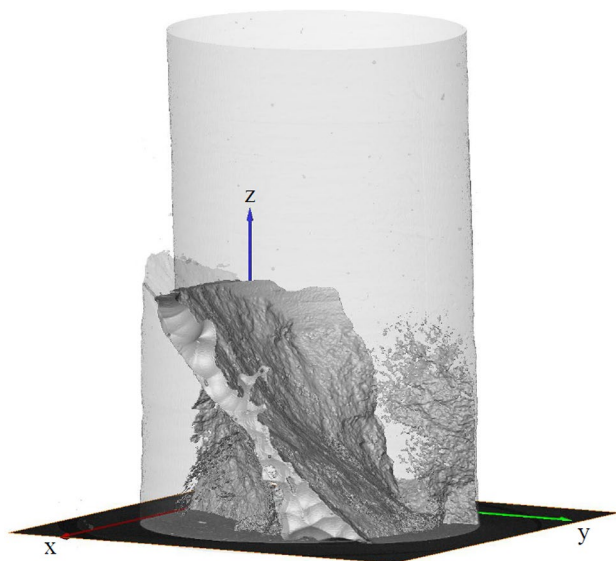


Fig. 10 Three-dimensional tomographic reconstruction of sample at failed state with main cracks inside lower half region

easy to give a definitive explanation of this quite localized cracking process. Two reasons can be invoked. Firstly, in spite that two translucent polycarbonate bases are used to support the sample, frictional forces still exist between the sample and bases. There is a stress concentration around the lower and upper surfaces of sample. It is possible that the stress concentration of slightly stronger on the lower surface than on the upper one. Secondly, a number of small weak bands, corresponding to low-density soft minerals, are identified in the lower half region of sample through the scanned images and in particular around the bottom surface.

The mechanical strength of these weak minerals is generally lower than that of other ones. As a consequence, most induced cracks in the present case are located in the lower half region of sample. On the other hand, in the upper half region of sample, there is a big weak band perpendicular to the longitudinal axis. Although the weak band exhibits a large deformation under applied compressive stress, no cracks are formed in the band.

The tomographic reconstructed images presented here allow the observation of major strain localization and cracking processes, in particular around the failed state of sample. But they are not suitable to quantify the local strain field and to capture its progressive localization through different loading steps (Louis et al. 2006; Maire and Withers 2014). The micro-tomography images actually represent the current local mass density field, which is related to local volumetric deformation. When the local deformation occurs under an isobaric condition, i.e. without volume change, it is invisible in tomographic images. In some cases, even a large volumetric strain is generated, the change of local mass density is not necessarily significant enough to be clearly observed in XMT images. Therefore, the Digital Volume Correlation based method should be used for the fine characterization of local strain localization. This will be performed and presented in Sect. 4.

3.2 Evolution of Averaged Strains

Due to the material heterogeneity, the small size of sample and the long duration of creep test, classical techniques for measuring strain such as gauges and displacement transducers are not appropriate for the strain measurement. Based on

highly contrasted 3D tomographic images, the DVC provides an efficient alternative procedure to quantitatively calculate the local displacement and strain fields. Indeed, by searching for the similitude between two images by considering the optic flow conservation, the displacement vector of the selected point can be determined (Bornert 2010). The local strain field can then be calculated from the displacement field. This method is here used to compute the local creep strain field inside the claystone sample. In order to represent the macroscopic responses of each tested sample, the average strains are also calculated by making volumetric averaging of the local strain field.

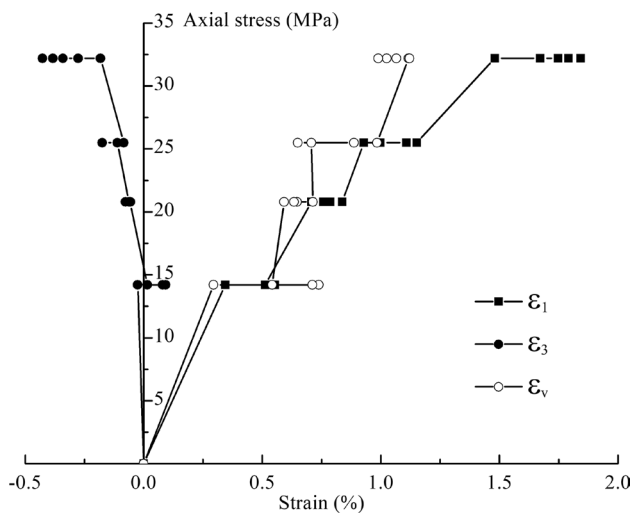


Fig. 11 Average axial, radial and volumetric strains of sample versus axial stress in the creep test

The calculation of the radial strain is completed in the cylindrical coordinate system. First the calculation zone in the sample is defined by using a 3D mask. Then the centre of the circle of each slice is found by Hough Circles Transformation. Finally the value of the radial strain is obtained by transforming the results of the calculation from the space Cartesian coordinate system into the cylindrical coordinate system ($\epsilon_3 = \sqrt{\epsilon_x^2 + \epsilon_y^2}$, x and y directions being orthogonal in the space Cartesian coordinate system).

As an example, in Fig. 11, one shows the curves of average axial (ϵ_1) and radial strains (ϵ_3) versus the axial stress for a representative creep test. The volumetric strain ($\epsilon_v = \epsilon_1 + 2\epsilon_3$) is also given in this figure. The horizontal parts of strain curves with a constant value of axial stress represent the strains induced by claystone creep process. The corresponding evolutions of strains with time are presented in Fig. 12. As mentioned above, all strain values in Figs. 11 and 12 are obtained by the volumetric averaging of local strain fields issued from the DVC computations.

From the results obtained, one observes first that the increases of compressive axial stress at all loading steps produce instantaneous compressive strain increments in the axial direction and tensile ones in the radial direction. But the instantaneous tensile radial strain increments are very small for the first two loading steps. This indicates very small values of Poisson’s ratio if the mechanical behavior of claystone is assumed to be elastic. Then, under constant values of axial stress, significant creep strains are observed for all loading steps. In general, the amplitude of both axial and radial creep strains increases when the applied axial stress is higher. The creep strains under the

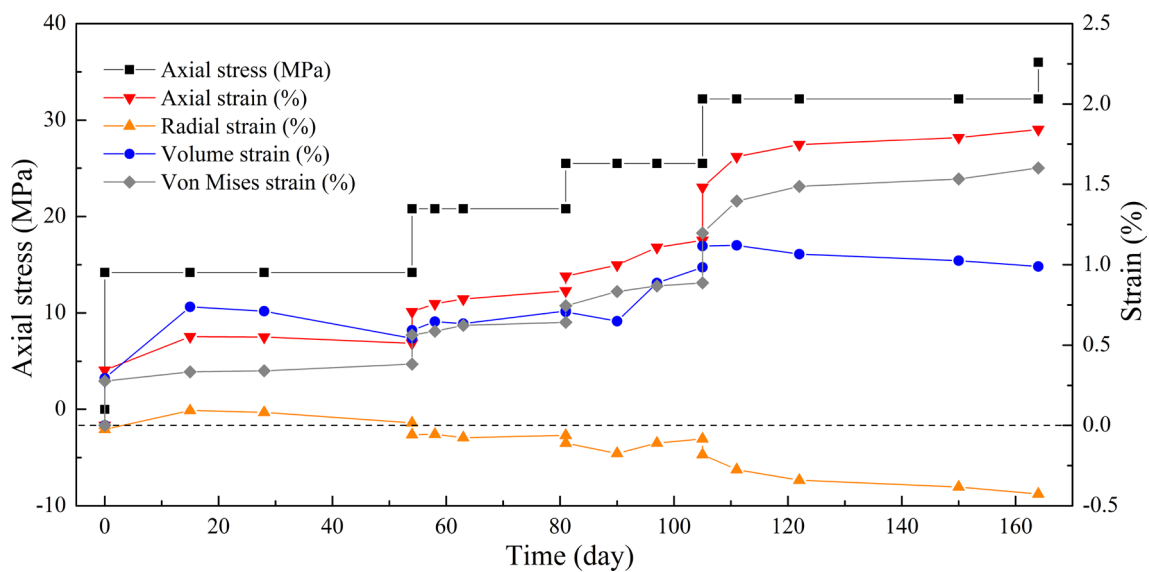


Fig. 12 Evolutions of different average strain components with time during a typical creep test

low stress levels, at the first to the third loading steps, tend to stabilize in 2 to 3 weeks. Due to the direct effect of compressive axial stress, compressive axial creep strain increments are obtained for all the steps. However, the variations of radial creep strain seems to be more complex than those of axial one. More precisely, during the first creep step, the radial creep strain first evolves slightly in compaction before increasing in extension. During the second and third creep steps, the variations of tensile radial strain are very small. When the axial stress reaches about 90% of the estimated uniaxial compression strength at the fourth step, the radial creep strain increases continuously in extension during almost 2 months. Several underlying mechanisms can be involved in such complex evolution in particular in the compaction-extension transition. One of those could be the pore compaction during creep process. Indeed, it is believed that inelastic deformation of COx claystone mainly occurs in the porous clay matrix (Wang et al. 2015; Pardoen et al. 2020). Due to the presence of pores and under compressive axial stress, the collapse of pores can induce compressive strains even in the radial direction. However, further investigations at the pores scale are needed for an in-depth understanding of complex creep deformation mechanisms of the COx claystone. On the other hand, it is interesting to observe that the variation of volumetric creep strain ($\Delta\varepsilon_v$) shows a continuous increase in extension during the fourth creep step. This volumetric dilation can be related to the initiation and propagation of cracks presented above.

For the sake of completeness, the so-called von Mises equivalent strain (ε_{eq}) is evaluated. This scalar valued strain variable is calculated from differences between three principal strains and then used to especially represent the intensity of shearing deformation. This equivalent shear strain is used to easily illustrate the strain localization process in the tested sample. The obtained values are also presented in Fig. 12. It is interesting to remark that the equivalent shear strain is smaller than the volumetric one during the first creep step, almost equal to during the second and third steps and larger during the fourth step. That means the difference between the axial and radial creep strains becomes more and more large when the axial stress is higher. Therefore, it seems that the creep process under uniaxial compression loading produces an important shearing deformation in the COx claystone. This shearing deformation can be related to sliding along bedding planes.

Finally, for the creep test shown in Fig. 11, the sample fails at 36 MPa before reaching the last loading step, i.e. 95% of the estimated uniaxial compression strength. Therefore, only the creep strains during the first four loading steps are presented.

4 Analysis of Local Strain Field

4.1 Strain Field in Whole Sample

With the help of the DVC, the full strains fields in the tested sample are calculated. For the sake of reducing figure number, the von Mises equivalent strain is then calculated from the different strain components. In this study, 17 strain maps at different values of axial stress and different time steps are determined and presented in Figs. 13 and 14. From these results, it is obvious that the creep strain field of the sample is not uniformly distributed. More precisely, the creep strain fields show some layered distribution. It is recalled that in this study, the sample tested is drilled in the perpendicular direction to the bedding planes of COx claystone. Therefore, the applied axial stress is perpendicular to those bedding plane. From the strain maps obtained, one can identify a series of almost regularly spaced horizontal strain concentration bands. These bands are then parallel to the bedding planes. That indicates that there are a series of horizontal weak material zones in the claystone sample. These weak zones can be related to weak clay zones with a small content of quartz and calcite grains or with a high porosity. It is worth noticing that under uniaxial compression loading, the compaction of axial strain is an essential process. It could be then interesting to present the distributions of axial strain. However, to limit figure number, only the distributions of von Mises strain are selected in this paper as it corresponds to the difference between axial and radial strains and it is a good variable to show the progressive localization process of strains. But as the axial strain is much larger than the radial one (as indicated in Fig. 12), the general distributions of axial strain and von Mises one are quite similar, with the formation of sub-horizontal localization bands.

One can also observe a number of isolated small strain concentration zones. These strain localization zones can be related to high plastic deformation around stiff calcite and quartz grains. This kind of strain localization process has been reported in some previous results with 2D image correlation (Wang et al. 2015; Yang et al. 2013).

On the other hand, the strain concentration zones mentioned above become more and more pronounced with the increase of axial stress. More interestingly, for a fixed value of axial stress, the strain field continues to evolve due to creep process of claystone. For instance, from the state $\sigma_1=25.5$ MPa (Fig. 14d) and $t = 81$ days to $\sigma_1 = 25.5$ MPa and $t = 105$ days (Fig. 14g), the amplitude of strain is increased and the strain localization process is enhanced. At the last step of loading ($\sigma_1=32.7$ MPa), one observes a number of small zones (red color) with a strain value close to 5%. The heterogeneity of the creep strain field

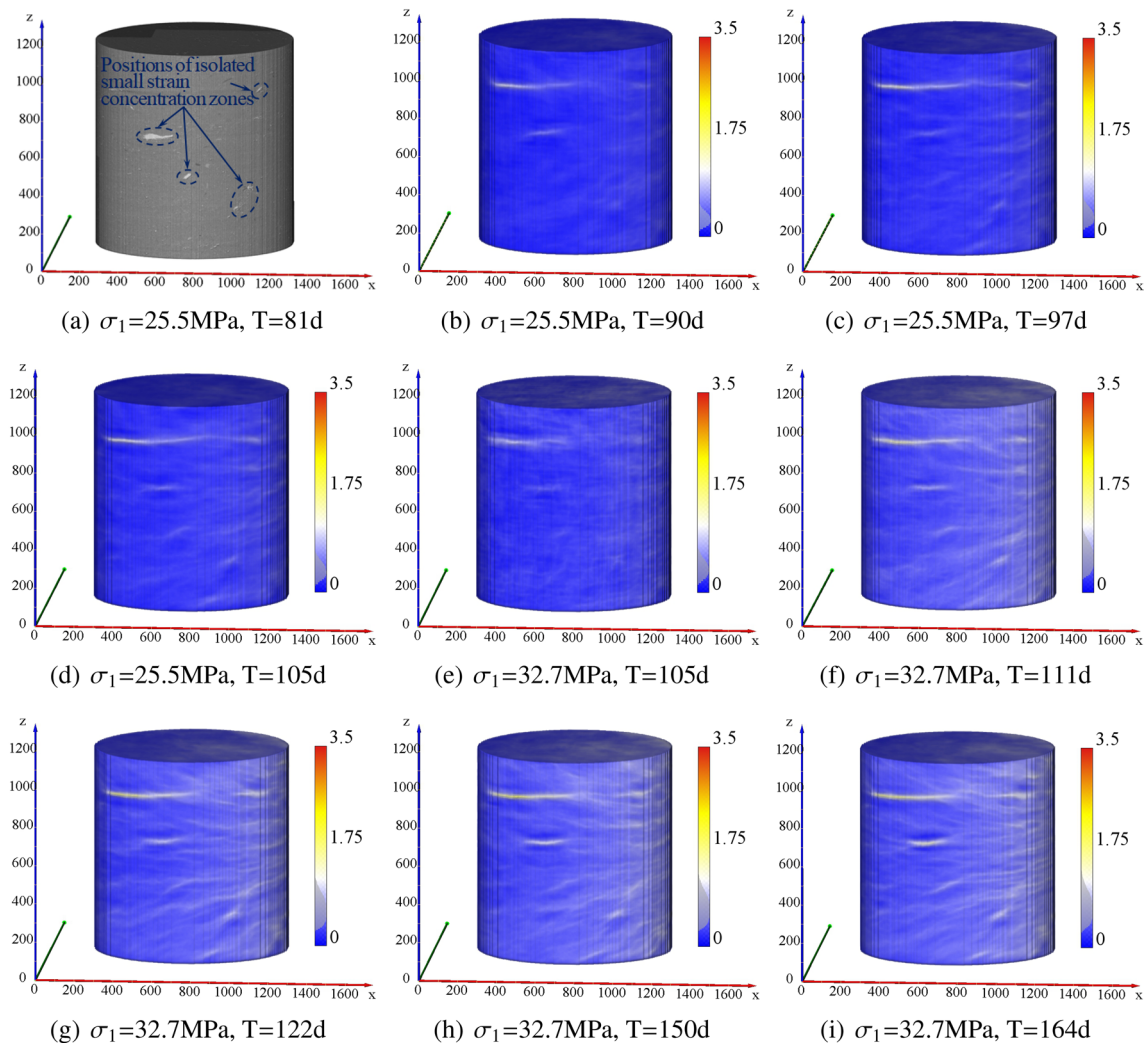


Fig. 13 Distribution of von Mises strain (in %) in the sample at different stress and time steps

in the sample becomes more and more marked. It suggests that the effect of stiff mineral inclusions (quartz and calcite) on the deformation process of claystone is more important at the high plastic strain range than at the small elastic strain range. However, the overall creep strain fields presented here are not clearly correlated with the cracking process discussed in the previous section and do not allow the detailed investigation of strain concentration process around the stiff calcite and quartz grains. This issue is discussed in the next section.

4.2 Strain Field on a Selected Section

To obtain a closer view on the effect of stiff inclusions on the local deformation process of the claystone, the evolution of strain field for on the slice-910 (see Fig. 7) is here analyzed in a more detailed way. This slice is taken from a zone of the

sample where a high content of stiff inclusions is found and a strong strain concentration is observed.

In Fig. 15, one shows the reconstructed tomographic image of the slice 910. The enlarged image on the right gives a view of a selected local zone. The blue colored areas represent the low-density materials, for instance, the clay matrix with many small pores. On the contrary, the white colored areas correspond to the high-density materials, mainly the heavy minerals such as pyrite and siderite. These mineral particles represent the stiff inclusions with respect to the clay matrix.

The maps of von Mises strain on this slice are presented in Fig. 16 for the different values of axial stress and creep time. Consistent with the results presented in the 3D maps of Fig. 13, the strain field on the selected slice clearly increases with the rise of applied axial stress and with creep time for the same value of stress. Further, there are more and more concentrated strain zones in the upper part of the section.

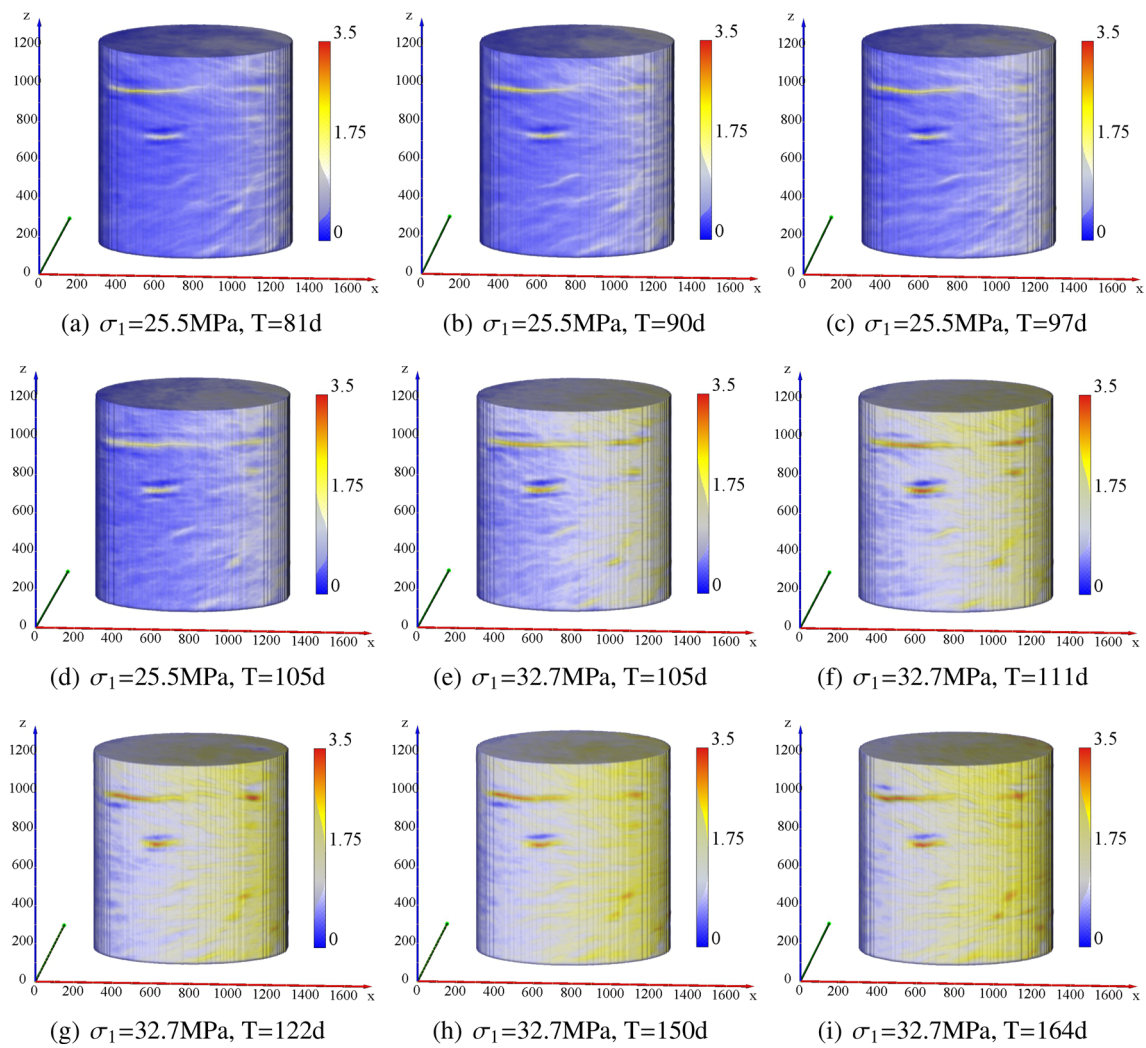
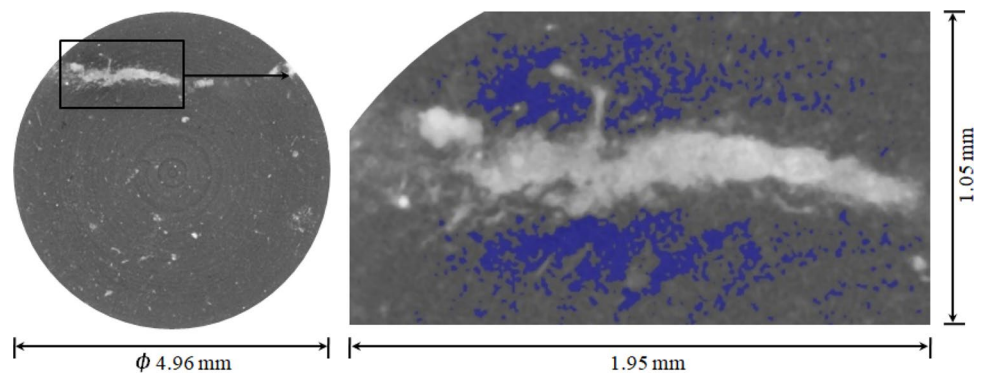


Fig. 14 Distribution of von Mises strain (%) in the sample at different stress and time steps

Fig. 15 A partial enlarged view of the soft hard inclusions on the slice-910 at the initial state (the blue colored areas represent the low-density materials)



This deformation pattern can be related to the microstructure shown in Fig. 15.

Indeed, it can be observed that the local strains of the low density areas (blue colored) increase quickly and become much higher than those in high density ones. Moreover,

the strain concentration is the most important in the low-density areas round the stiff inclusions (white colored). For instance, even at a relatively low axial stress (40% of the uniaxial compression strength, i.e. 14.2 MPa), the strains in those areas are already several times higher than that in other

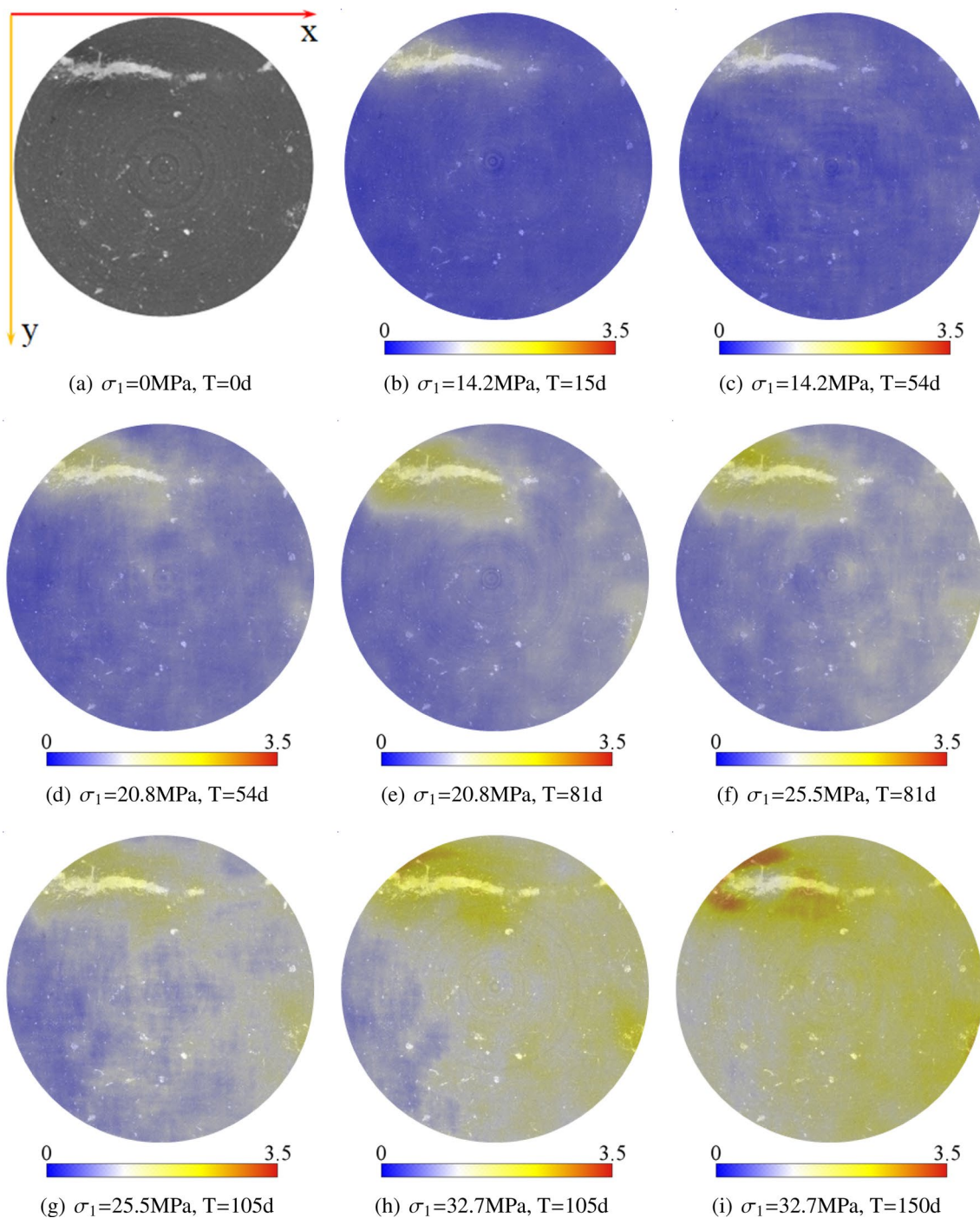


Fig. 16 Evolutions of von Mises strain field on the selected slice-910 at different values of axial stress and creep time

regions. Therefore, it seems that the presence of stiff inclusions enhances the local strain concentration in the weak porous clay matrix. This should be probably related to the local stress concentration inside the interface zones between the soft clay matrix and stiff inclusions.

On the other hand, the strain field on the selected slice exhibits a clear asymmetry with respect to the sample axis

(z -axis). More precisely, the strain along x -axis is significantly different with that along y -axis. For instance, starting from the sample center point, the strain in the right half part is clearly smaller than that in the left one. This results suggest that the classical axi-symmetry assumption adopted in most macroscopic tests on cylindrical samples is not verified by the local strain field. This dissymmetry can be related

to two reasons: the first one is the material heterogeneity as discussed above. The second one may be related to the parallelism of the tested sample and to the defect of the axial loading device. It is possible that the axial stress is not perfectly aligned to the sample axis and the upper and bottom surfaces of the sample are not strictly parallel. Therefore, a small bending of sample can be induced.

Finally, in Fig. 17, one shows the evolutions of von Mises equivalent strain on the slice at different instances of creep time under a constant stress of 32.7 MPa. It is seen that the strain level progressively increases with the creep time (from 105 to 122 days) mainly in the low-density areas around the stiff inclusions in the upper half part of the cross-section. The strain concentration is intensified during this period. However, after 122 days of creep, it seems that there is a diffusion of creep strain through all the cross-section. This evolution of creep strain field can be related to the complex interaction process between stiff inclusions and soft clay matrix. Indeed, the strong heterogeneity of local strain field, in particular during the phase of increasing applied stress, is directly induced by the material heterogeneity. When the applied stress is raised, a strong stress concentration is generated inside the neighboring zones between the stiff inclusions and clay

matrix due to the difference in elastic modulus between the different materials. This stress concentration induces a strong strain localization in those zones. The larger the volume fraction of stiff inclusions, the more significant the stress and strain concentration. The greater the difference of elastic modulus between the stiff inclusion and clay matrix, the greater the stress and strain concentration effects. However, when the applied stress is held constant during the creep phase, the stress concentrations are progressively relaxed with the creep deformation of clay matrix. As a consequence, the strain contrast is progressively attenuated (from 122 to 164 days) and the local strain field tends to become more and more uniform. But some local concentrated strain zones can still be observed. Finally, in Fig. 18, the distributions of von Mises equivalent strain on the longitudinal section along the sample axis are presented for different instances of creep time at the loading step of 32.7 MPa. In accordance with 3D distributions, one observes a layer-like distribution of strain and the progressive formation of horizontal strain concentration bands. These results seem to confirm that the creep deformation in the COx claystone is related to the compaction of bedding planes.

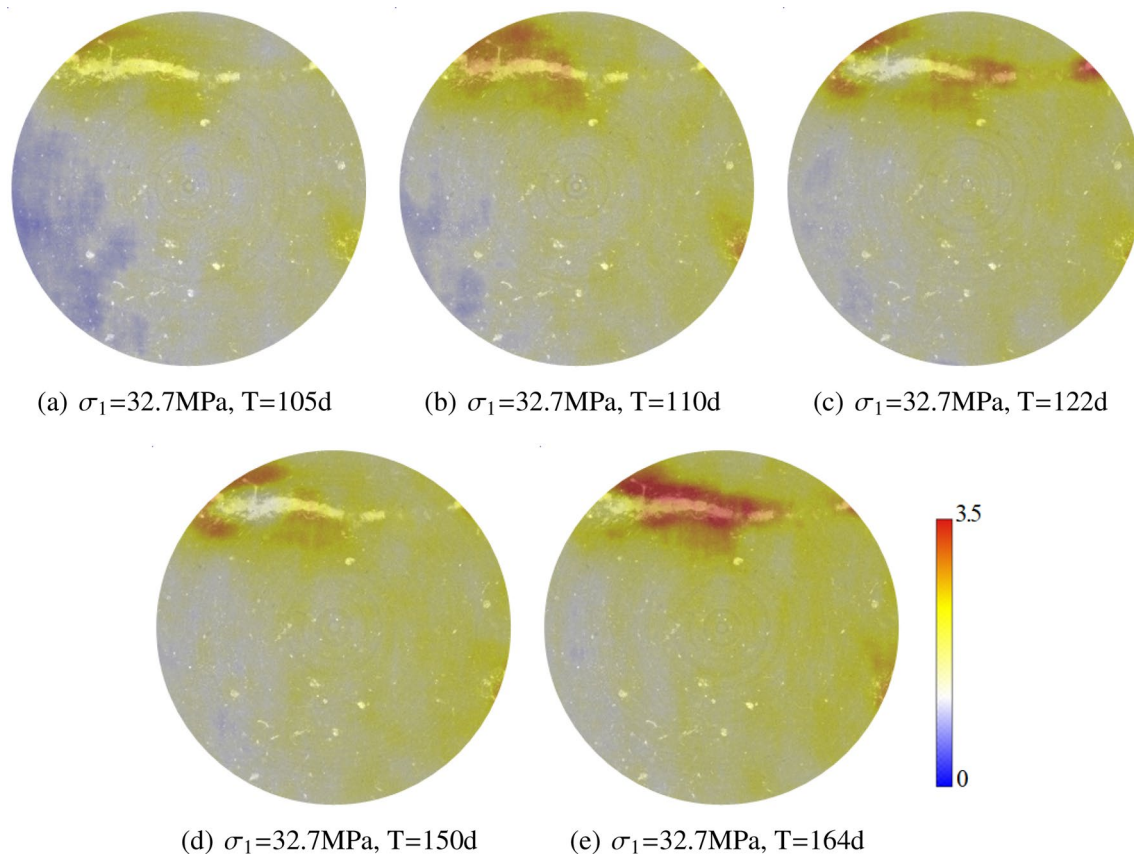


Fig. 17 Evolutions of von Mises strain on the slice 910 under the axial stress of 32.7 MPa and at different instances of creep time

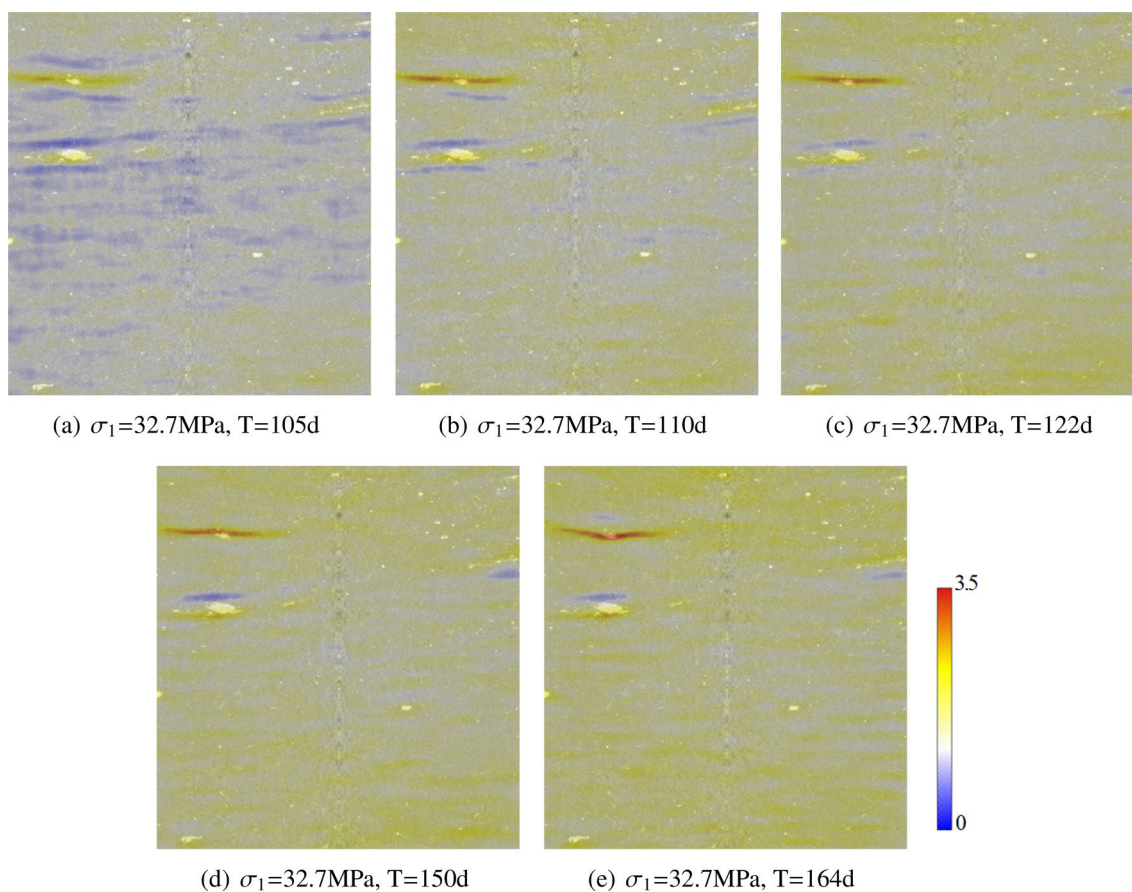


Fig. 18 Evolutions of von Mises strain on the longitudinal section (parallel to cylinder axis) under the axial stress of 32.7 MPa and at different instances of creep time

5 Conclusions

In this study, in situ creep tests have been performed on the COx claystone under uniaxial compression stress by using a new experimental device. The deformation of the tested sample during stress loading and creep process was monitored by using X-ray micro-tomography. Three-dimensional strain fields inside the tested sample have been determined by using a digital volume correlation (DVC) method. The obtained results lead to the following main remarks.

The micro-tomography imaging combined with 3D image correlation technique is able to accurately determine the full strain field in tested sample. This method is particularly powerful for long time tests and for strongly heterogeneous materials for which most classical methods generally failed.

The local strain field in the COx claystone is strongly heterogeneous and the strain heterogeneity is inherently related to material heterogeneity. Due to the difference of elastic properties between stiff inclusions and soft clay matrix, under the applied axial stress, a strong stress concentration occurs inside the inclusion-matrix interfaces

zones and this leads to an important strain concentration. The low-density zones around the stiff inclusions exhibit a much higher strain than the other zones. With the creep deformation of clay matrix under a constant stress, the stress concentration is progressively relaxed and the whole strain field becomes more and more uniform.

The cracking process leading to the macroscopic failure of sample occurs rather in a sudden manner. Multiple cracks can be generated and they are essentially located in the zones of materials with weak mechanical strength.

The COx claystone is an anisotropic material. It will be useful to investigate the effects of material anisotropy on the creep behavior by performed similar tests with other loading orientations.

Acknowledgements The present study was jointly supported by Andra and the ISIS4D X-Ray CT platform. This platform has been funded by the International Campus on Safety and Inter-modality in Transportation (CISIT), the Hauts-de-France Region, the European Community and the National Center for Scientific Research (CNRS). Special thanks are addressed to Jean-Pierre Parent and Jean Secq for their invaluable assistance to the design of experimental device and preparation of samples.

References

- Armand G, Conil N, Talandier J, Seyedi DM (2017) Fundamental aspects of the hydromechanical behaviour of Callovo–Oxfordian claystone: from experimental studies to model calibration and validation. *Comput Geotech* 85:277–286
- Armand G, Leveau F, Nussbaum C, deLaVaissiere R, Noiret A, Jaeggi D, Landrein P, Righini C (2014) Geometry and properties of the excavation induced fractures at the meuse-haute-marne url drifts. *Rock Mech Rock Eng* 47:21–41
- Bauer A, Verhulp E, Schoofs S (2006) Measuring local strains in sandstones under stress with microcomputed tomography. In: *Advances in x-ray tomography for geomaterials*, pp 247–253
- Bennett KC, Berla LA, Nix WD, Borja RI (2015) Instrumented nanoindentation and 3d mechanistic modeling of a shale at multiple scales. *Acta Geotech* 10:1–14
- Besnard G, Hild F, Roux S (2006) Finite element displacement fields analysis from digital images application to portevin le chatelier bands. *Exp Mech* 46:789–803
- Bornert M (2010) X-ray micro ct for studying strain localization in clay rocks under triaxial compression. In: *Advances in X-ray tomography for geomaterials*, vol 118, pp 35–52
- Buljac A, Jailin C, Mendoza A, Neggers J, TaillandierThomas T, Bouterf A, Smaniotto B, Hild F, Roux S (2018) Digital volume correlation review of progress and challenges. *Exp Mech* 58:661–708
- Chen G, Maes T, Vandervoort F, Sillen X, Van Marcke P, Honty M, Dierick M, Vanderniepen P (2014) Thermal impact on damaged boom clay and opalinus clay: permeameter and isostatic tests with μ ct scanning. *Rock Mech Rock Eng* 47(1):87–99
- Chu T, Ranson W, Sutton MA (1985) Applications of digital-image-correlation techniques to experimental mechanics. *Exp Mech* 25(3):232–244
- Desbois G, Hohne N, Urai JL, Besuelle P, Viggiani G (2017) Deformation in cemented Mudrock (Callovo–Oxfordian clay) by microcracking, granular flow and phyllosilicate plasticity: insights from triaxial deformation, broad ion beam polishing and scanning electron microscopy. *Solid Earth* 8(2):291–305
- Desrues J, Viggiani G, Besuelle P (2010) *Advances in X-ray tomography for geomaterials*, vol 118. Wiley, New York
- Gasc-Barbier M, Chanchole S, Berest P (2004) Creep behavior of bure clayey rock. *Appl Clay Sci* 26:449–458
- Hu DW, Zhang F, Shao JF, Gatmiri B (2014) Influences of mineralogy and water content on the mechanical properties of argillite. *Rock Mech Rock Eng* 47:157–166
- Kak AC, Slaney M (2001) Principles of computerized tomographic imaging. *Classics in applied mathematics*, vol 33. Society for Industrial and Applied Mathematics, Philadelphia
- Kawakata H, Cho A, Kiyama T, Yanagidani T, Kusunose K, Shimada M (1999) Three dimensional observations of faulting process in westerly granite under uniaxial and triaxial conditions by x-ray ct scan. *Tectonophysics* 313(3):293–305
- Lenoir N, Bornert M, Desrues J, Besuelle P, Viggiani G (2007) Volumetric digital image correlation applied to x-ray microtomography images from triaxial compression tests on argillaceous rock. *Strain* 43(3):193–205
- Li Z, Limodin N, Tandjaoui A, Quaegebeur P, Witz J-F, Balloy D (2017) Influence of Fe content on the damage mechanism in a319 aluminum alloy: tensile tests and digital image correlation. *Eng Fract Mech* 183:94–108
- Limodin N, Rougelot T, Hosdez J (2013) Isis4d—in situ innovative set-ups under x-ray microtomography. <http://isis4d.univ-lille.fr>
- Liu ZB, Shao JF, Liu TG, Xie SY, Conil N (2016) Gas permeability evolution mechanism during creep of a low permeable claystone. *Appl Clay Sci* 129:47–53
- Liu ZB, Shao JF, Xie SY, Conil N, Talandier J (2019) Mechanical behavior of claystone in lateral decompression test and thermal effect. *Rock Mech Rock Eng* 52:321–334
- Liu ZB, Shao JF, Xie SY, Conil N, Zha WH (2018) Effects of relative humidity and mineral compositions on creep deformation and failure of a claystone under compression. *Int J Rock Mech Min Sci* 103:68–76
- Liu ZB, Shao JF, Xie SY, Secq J (2015) Gas permeability evolution of clayey rocks in process of compressive creep test. *Mater Lett* 139:422–425
- Liu ZB, Xie SY, Shao JF, Conil N (2015) Effects of deviatoric stress and structural anisotropy on compressive creep behavior of a clayey rock. *Appl Clay Sci* 114:491–496
- Louis L, Wong T-F, Baud P, Tembe S (2006) Imaging strain localization by x-ray computed tomography: discrete compaction bands in diemelstadt sandstone. *J Struct Geol* 28(5):762–775
- Maire E, Withers PJ (2014) Quantitative x-ray tomography. *Int Mater Rev* 59(1):1–43
- Mao L, Zhu Y, Wang Y, Liu Y, Li L, Chiang F-P (2019) An improved digital volumetric speckle photography technique with x-ray microtomography and its applications to investigating strain localization in red sandstone. *Rock Mech Rock Eng* 1–10 (**in press**)
- Menaceur H, Delage P, Tang AM, Conil N (2015) The thermo-mechanical behaviour of the Callovo–Oxfordian claystone. *Int J Rock Mech Min Sci* 78:290–303
- Otani J, Mukunoki T, Obara Y (2000) Application of x-ray ct method for characterization of failure in soils. *Soils Found* 40(2):111–118
- Pardoën B, Bésuelle P, Dal Pont S, Cosenza P, Desrues J (2020) Accounting for small-scale heterogeneity and variability of clay rock in homogenised numerical micromechanical response and microcracking. *Rock Mech Rock Eng* 1–20 (**in press**)
- Robinet JC, Sardini P, Coelho D, Parneix JC, Pret D, Sammartino S, Boller E, Altmann S (2012) Effects of mineral distribution at mesoscopic scale on solute diffusion in a clay-rich rock: example of the callovo-Oxfordian mudstone (bure, france). *Water Resour Res* 48:W05554
- Stavropoulou E, Ando E, Roubin E, Lenoir N, Tengattini A, Briffaut M, Besuelle P (2020) Dynamics of water absorption in callovo-oxfordian claystone revealed with multimodal x-ray and neutron tomography. *Front Earth Sci* 8:6. <https://doi.org/10.3389/feart.2020.00006>
- Stock SR (2008) Recent advances in x-ray microtomography applied to materials. *Int Mater Rev* 53(3):129–181
- Viggiani G, Besuelle P, Desrues J (2013) X-ray micro tomography as a tool for studying localized damage/deformation in clay rock. *Tech. Rep. 1*
- Viggiani G, Lenoir N, Bésuelle P, Michiel M, Marello S, Desrues J, Kretzschmer M (2004) X-ray microtomography for studying localized deformation in fine-grained geomaterials under triaxial compression. *Comptes rendus Mécanique* 332(10):819–826
- Wang L, Limodin N, El Bartali A, Witz J-F, Seghir R, Buffiere J-Y, Charkaluk E (2016) Influence of pores on crack initiation in monotonic tensile and cyclic loadings in lost foam casting a319 alloy by using 3d in-situ analysis. *Mater Sci Eng A* 673:362–372
- Wang LL, Bornert M, Heripre E, Chanchole S, Pouya A, Halphen B (2015) The mechanisms of deformation and damage of mudstones: a micro-scale study combining esem and dic. *Rock Mech Rock Eng* 48:1913–1926
- Yang DS, Chanchole S, Valli P, Chen LF (2013) Study of the anisotropic properties of argillite under moisture and mechanical loads. *Rock Mech Rock Eng* 46:247–257
- Yang S-Q, Ju Y, Gao F, Gui Y-L (2016) Strength, deformability and x-ray micro-ct observations of deeply buried marble

under different confining pressures. *Rock Mech Rock Eng* 49(11):4227–4244

Zhang F, Xie SY, Hu DW, Shao JF, Gatmiri B (2012) Effect of water content and structural anisotropy on mechanical property of claystone. *Appl Clay Sci* 69:79–86

Publisher's Note Springer Nature remains neutral with regard to jurisdictional claims in published maps and institutional affiliations.